TU Delft

Delft University of Technology

Spatiotemporal operando UV–vis spectroscopy

Development and mechanistic alternation of CO oxidation on Pt/Al_2O_3 on the reactor scale

van Beek, Louise; Jain, Disha; Gholkar, Pratik; Eldridge, Thomas J.; Nguyen, Hai P.; Muramoto, Kei; Urakawa, Atsushi

DOI
10.1016/j.cattod.2023.114466

Publication date
2024

Document Version
Final published version

Published in
Catalysis Today

Citation (APA)
van Beek, L., Jain, D., Gholkar, P., Eldridge, T. J., Nguyen, H. P., Muramoto, K., & Urakawa, A. (2024). Spatiotemporal operando UV–vis spectroscopy: Development and mechanistic alternation of CO oxidation on Pt/Al_2O_3 on the reactor scale. *Catalysis Today*, *429*, Article 114466. https://doi.org/10.1016/j.cattod.2023.114466

Important note
To cite this publication, please use the final published version (if applicable).
Please check the document version above.

Copyright
Other than for strictly personal use, it is not permitted to download, forward or distribute the text or part of it, without the consent of the author(s) and/or copyright holder(s), unless the work is under an open content license such as Creative Commons.

Takedown policy
Please contact us and provide details if you believe this document breaches copyrights.
We will remove access to the work immediately and investigate your claim.

This work is downloaded from Delft University of Technology.
For technical reasons the number of authors shown on this cover page is limited to a maximum of 10.

Catalysis Today 429 (2024) 114466

Contents lists available at ScienceDirect

Catalysis Today

journal homepage: www.elsevier.com/locate/cattod

Spatiotemporal *operando* UV–vis spectroscopy: Development and mechanistic alternation of CO oxidation on Pt/Al_2O_3 on the reactor scale

Louise van Beek [a,c], Disha Jain [a], Pratik Gholkar [a], Thomas J. Eldridge [a], Hai P. Nguyen [b], Kei Muramoto [d], Atsushi Urakawa [a,*]

[a] Catalysis Engineering, Department of Chemical Engineering, Delft University of Technology, Van der Maasweg 9, 2629 Hz, Delft, the Netherlands
[b] Toyota Motor Europe, Hoge wei 33, B-1933 Zaventem, Belgium
[c] Université Grenoble Alpes, 621 avenue Centrale, Saint-Martin-d'Hères, France
[d] Toyota Motor Corporation, Mishuku 1200, Susono, Shizuoka, Japan

ARTICLE INFO

Keywords:
UV–vis
Diffuse reflection
operando
Space- and time-resolution
CO oxidation
Pt/Al_2O_3

ABSTRACT

Operando methodologies are widely used in heterogenous catalysis to understand unique state of catalyst materials emerging under specific reaction conditions and to establish catalyst structure-activity relationships. Recent studies highlight the importance of combining multiple *operando* techniques (multimodal approach) to gain complementary information as well as looking into chemical and material gradients and spatial variations on the reactor scale. In this work, we developed an *operando* UV–vis diffuse reflectance spectroscopy (DRS) setup compatible with a common fixed-bed tubular reactor. The design is based on optical calculations, validation experiments and signals considerations. A spatial resolution of 1 mm along the axial direction of the reactor was successfully demonstrated and combined with a time resolution of seconds with good signal to noise. CO oxidation over Pt/Al_2O_3 was performed as a proof of principle experiment demonstrating the capabilities of the new setup. The information gained by the space-resolved *operando* UV–vis DRS was combined with other space-resolved *operando* studies such as diffuse reflectance infrared Fourier transform spectroscopy (DRIFTS), gas sampling and temperature profiling. The study shows that the nature of active sites (Pt redox state) and thus the reaction mechanism alter with reaction temperature and also in space. Spatiotemporal UV–vis DRS is also demonstrated, showing the capability for transient studies with space-resolution.

1. Introduction

In heterogeneous catalysis, the states of active sites are widely explored and debated to enhance the understanding of reaction mechanisms and structure-activity relationships. Such detailed knowledge can be obtained through "real-time-in-action" experiments, which involve studying catalytic materials under *operando* conditions [1,2]. In other words, measurements are performed in-situ while the reaction is taking place. Alongside the significance of *operando* measurements, there is a growing consensus on the importance of investigating chemical gradients, such as fluid and surface species concentrations, redox state and catalyst structures as well as temperature in catalytic reactors to fully understand the catalytic activity observed at the reactor outlet. Such information requires space- and, in some cases, time-resolved measurements using multiple *operando* techniques (multimodal study) [3–6]. This is the field actively being developed, and expanding the repertoire of spatiotemporal *operando* tools is crucial for the catalysis community. It enables a more precise understanding of catalysis and facilitates the use of such information in designing next-generation catalytic material and processes.

Among *operando* methodologies, UV–vis diffuse reflectance spectroscopy (UV–vis DRS) is one of the fundamental investigation tools to study, for example, the coordination environment and redox state of transition metals and to investigate the formation of coke on active sites causing catalyst deactivation or serving as reaction intermediate [7–9]. The Praying Mantis diffuse reflection optical accessory in combination with the reaction chamber made by Harrick is the popular setup as reported by several groups to perform in-situ UV–vis spectroscopy in heterogeneous catalysis [10—14]. The optical cell enables measuring at high temperatures and collects about 20 % of the diffuse reflected light avoiding the collection of the specular reflection [15]. However, this configuration is designed to measure a fixed point of the catalyst bed.

* Correspondence to: Delft University of Technology Department of Chemical Engineering, Van der Maasweg 9, 2629 HZ Delft, Netherlands.
E-mail address: A.Urakawa@tudelft.nl (A. Urakawa).

https://doi.org/10.1016/j.cattod.2023.114466
Received 15 August 2023; Accepted 17 November 2023
Available online 21 November 2023
0920-5861/© 2023 The Author(s). Published by Elsevier B.V. This is an open access article under the CC BY license (http://creativecommons.org/licenses/by/4.0/).

Use of optical fibers overcame this spatial limitation and offered new possibilities to perform spatial- and time-resolved UV–vis DRS at the reactor scale. Thermally resistant optical-fiber reflection probes can be used to gain local (i.e., a fixed point of catalyst bed) information of catalyst materials and reaction intermediate in combination with other spectroscopic techniques [16–19] and multiple of such probes can be placed to acquire UV–vis spectra along the axial direction of a fixed-bed reactor [20–22]. The challenge of this configuration is the light collection efficiency of the reflection probe and also little flexibility geometrically to study various catalytic systems under varying conditions. Thus, it is desired to develop a UV–vis DRS configuration which allows high-sensitivity measurements while adapting a widely available UV–vis spectrometer such as a modular one.

In this work, we developed a UV–vis DRS tool capable of detecting material gradients inside a catalytic reactor. To ensure its applicability in kinetic studies, a tubular reactor was used while aiming at a spatial resolution of 1 mm and a time resolution of several seconds. Given the practical constraints, such as the tubular geometry and temperature of the catalytic reactor, we used long working-distance excitation and collection objectives coupled with optical fibers to the light source and spectrometer, respectively. Due to the inherently low luminosity of such a setup, we optimized all optical elements and paths to attain high light throughput (etendue) while respecting the 1 mm spatial resolution criterion. Additionally, to avoid the collection of specular reflection, the exciting and collection pathways were separated geometrically. The achievable time resolution with reasonable signal-to-noise (S/N) is heavily sample-dependent, and the choice of light source can compensate for weakly absorbing samples. Thus, two different light sources with distinct spectral and intensity characteristics were evaluated.

A proof-of-principle space-resolved (SR) UV–vis DRS study was performed with three colorful samples sequentially inserted in the reactor and by translating the sampling spot through the axial direction of the reactor. After confirming its functionality, on *operando* study on CO oxidation, a crucial reaction in automotive catalysis, was performed with Pt/Al_2O_3. While the reaction is considered simple, there are still ongoing debates regarding the active sites and reaction mechanisms. Notably, under specific reaction conditions, the active Pt can undergo oxidation, potentially leading to spatial and temporal alterations in the reaction mechanism. In this study, we demonstrate how the Pt redox state information gained by UV–vis DRS can offer vital insights to solve the puzzle of reaction mechanism. These results are supported by complementary reactor-scale space-resolved studies using diffuse reflectance infrared Fourier transform spectroscopy (DRIFTS), gas sampling and temperature measurements. Finally, the potential of the developed UV–vis DRS configuration for both space- *and* time-resolved studies is showcased by applying it to CO oxidation under unsteady-state operation wherein CO and O_2 are alternately passed through the reactor.

2. Development of space- and time-resolved UV–vis DRS

Light intensity of the signals of our interest, i.e., diffuse reflected light collected from the catalyst surfaces, and their spectral quality are influenced by multiple factors. We have chosen to consider the followings to achieve space- and time-resolved UV–vis DRS with maximized signal intensity and a spatial resolution of 1 mm:

(i) Collection of diffuse reflection based on the angles of incident and reflected light
(ii) Magnification to define the size of the sampling area, i.e., spot size of the diffuse reflected light
(iii) Throughput optimization to enhance light collection efficiency defined by the relationship between optical system, which includes optical fiber diameter and light divergence, and light intensity at the detector
(iv) Signal-to-noise (S/N) due to the choice of light sources and measurement parameters such as integration time and spectral averaging

In this section, we describe the theoretical background of (i)-(iv) relevant to design our space- and time-resolved UV–vis DRS setup, followed by the description of the actual sampling configuration and proof-of-principle space-resolved experiments.

2.1. Collection of diffuse reflection

When an incident light irradiates the material's surface with an angle of incidence α, two types of reflection can occur, namely specular and diffuse reflection (Fig. 1). By its definition, specular reflection leaves the surface at the same angle to the normal plane as the incident light. The specular reflected light is characterized by its brightness since it does not undergo diffuse reflection on the material surface and the light trajectory is well defined, easing the light collection. However, for catalysis research, specular reflected light often contains little information about the catalyst due to small penetration. On the contrary, the diffuse reflected light has a weak intensity at a specific light collection point, which makes the light collection challenging. If the catalyst surface is supposed to be Lambertian, i.e., ideal diffuse reflection, the reflected light leaves the surface with an angular distribution that is independent of the angle of incidence α. For most cases in catalysis, rough surfaces are dealt and thus diffuse-scattered light contains rich information on the catalyst materials and adsorbates, while specular-reflected light contains only the external surface information. Hence maximizing the diffuse reflected light is crucial and that is the aim of the unique designs in the commercial optical accessories.

To avoid the collection of specular reflection, the detector can be placed at any angle that is different from the angle of incidence α. For example, the contribution of specular reflected light is excluded by simply fixing the light collection system perpendicularly to the surface as shown in Fig. 1. This configuration enables to collect only the diffuse reflected light.

2.2. Magnification of the collection of the light

To add spatial resolution, a deliberate choice was made to monitor the spot size of the collected light rather than focusing the incident light on a small spot. Improper focusing of the incident light would result in reduced intensity and consequently weakening the intensity of the diffuse reflection at the detector. Therefore, the magnification of the light collection is employed to prevent great loss of light intensity. However, simple use of optical fibers for guiding and gathering the incident and reflected light is not sufficient to obtain a small spot size. In this work, two thin-lenses positioned between the catalytic bed and the

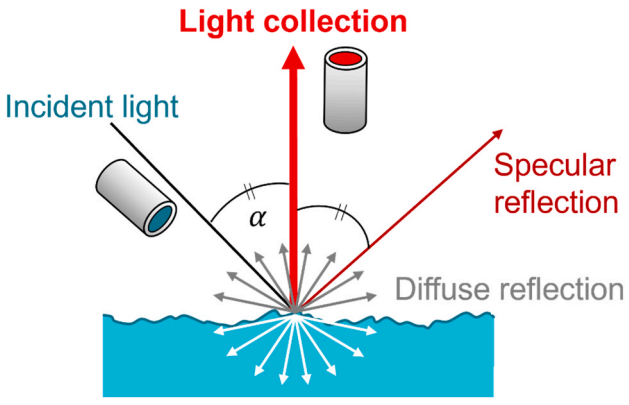

Fig. 1. Specular vs. diffuse reflection, and angular configuration to collect diffuse reflection in this work.

probe were used. These lenses define the spot size of 1 mm while achieving efficient collection of the diffuse reflected light.

Fig. 2 presents the design principle of our optical system. The rays leave the fiber exit with a divergence angle θ_{max} (also called acceptance angle [23]) and are aligned parallel to the direction of the propagation of the rays by the collimating lens (L_1). The parallel rays are focused by a plano-convex lens (L_2) which is placed at a distance (d) from L_1. This lens combination defines the transverse magnification of the optical system (M_T). Therefore, M_T is determined by the combination of the two lenses, lens characteristics (focal points, F_1,F_2), the positions of the fiber exit and sample along the direction of the propagation of the rays (s_{o1}, s_{i2}). Finally, the spot-size ($ØS$) is defined by the fiber diameter ($ØD$) and transverse magnification (M_T).

M_T is determined by the product of the transverse magnification of the collimating lens, M_{T1}, and the plano-convex lens, M_{T2}. By definition [23], the transverse magnification of L_1 and L_2 is equal to $M_{T1} = -\frac{s_{i1}}{s_{o1}}$ and $M_{T2} = -\frac{s_{i2}}{s_{o2}}$ where s_{oj} is called as the object distance and s_{ij} as the image distance $(j = 1, 2)$. Based on the Gaussian lens formula (Eq. (1)) the focal length $f_j (j = 1, 2)$ can be calculated as follows.

$$\frac{1}{f_j} = \frac{1}{s_{oj}} + \frac{1}{s_{ij}} (j = 1, 2) \tag{1}$$

The image distance s_{i1} can be expressed according to f_1, $s_{i1} = \frac{s_{o1} f_1}{s_{o1} - f_1}$, and the object distance s_{o2} according to d, $s_{o2} = d - s_{i1}$.Thus, the transverse magnification of the thin-lens combination is equal to the following.

$$M_T = \frac{f_1 s_{i2}}{d(s_{o1} - f_1) - s_{o1} f_1} \tag{2}$$

The response of the optical system can be computed by equation (2) depending on the configuration of the optical system to determine the spot size $ØS$,

$$ØS = M_T \times ØD \tag{3}$$

2.3. Throughput calculations

Section 2.2 explains how a desired spot-size can be achieved by thin lens combination and fiber diameter. However, the light collection efficiency may not be sufficient to obtain high S/N influencing the measurement time and thus the time-resolution of UV–vis DRS. For this reason, the light collection efficiency needs to be optimized in order to maximize the intensity of the diffuse reflected light collected. The throughput (G) (also named as geometrical extend, optical extend, optical invariant, or etendue) can be calculated in such cases to quantify the radiant flux given, for example, at the entrance and exit of optical fibers and apertures of lenses. G calculations applied to every optical component in the OS enable to target which component will limit the maximum radiant flux by identifying which component has the smallest G value. The smaller the G value is, the less light will come in and out of the given component. Therefore, the light collection efficiency of the system can only be enhanced by increasing the smallest G value of the identified optical component. The throughput is used in radiometric analysis to design efficient light coupling optical system (OS) [24]. Designing high-throughput OS to enhance the resolution of spectroscopical methods has been done previously applied to Raman spectroscopy by Hug and Hangartner [25] and by Meade et al. [26] and applied to interferometric spectroscopy by Wang et al. [27].

The present OS is simply constituted by thin lenses and optical fibers both defined by their divergence angle θ_{max} (*see* Section 2.2, geometrical parameter indicating an angular limit for the rays to enter and exit) [23]. The light-gathering capabilities of optical components are determined by θ_{max} via the numerical aperture (NA) and f-number (f/#) specific to optical fibers and thin-lenses, respectively. Usually, NA is provided by the supplier and can be calculated as,

$$NA = \sqrt{n_f^2 - n_c^2} \tag{4}$$

with the refractive index of the cladding n_c and the core n_f. Based on the

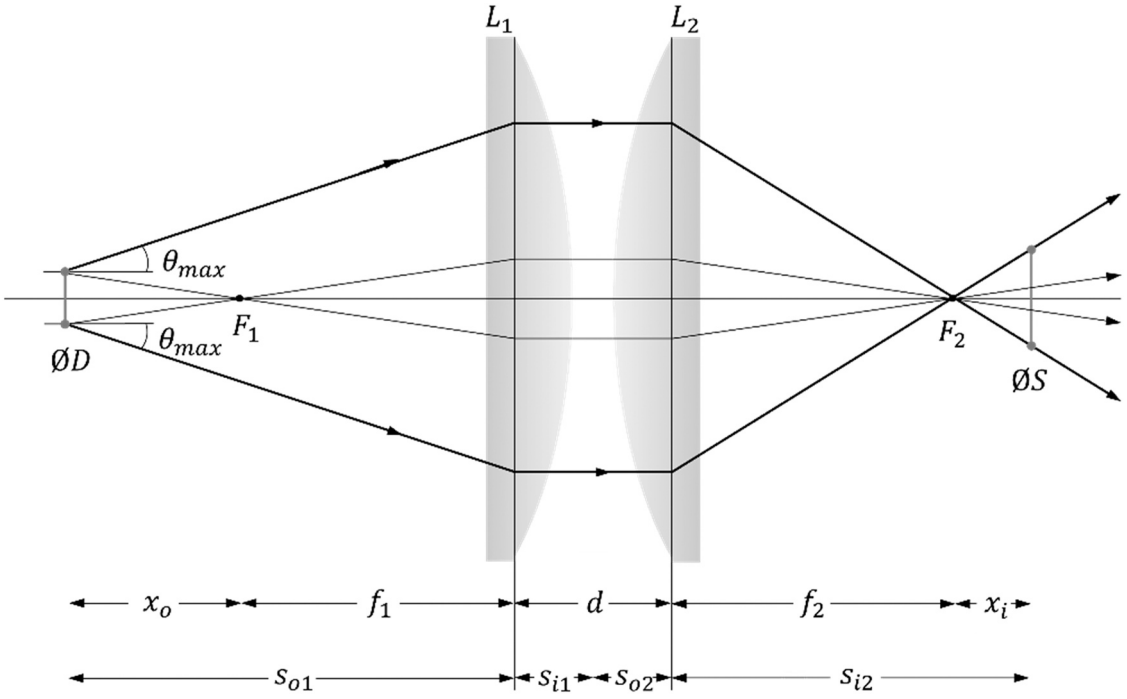

Fig. 2. Thin-lens combination of a collimating lens L_1 and a plano-convex lens L_2 separated by a distance d. F_1 and f_1 are L_1 focal point and focal length, respectively. F_2 and f_2 are L_2 focal point and focal length respectively. At the fiber exit, characterized by the fiber diameter $ØD$, the rays diverge with an angle θ_{max}. The fiber exit is placed at the object distance s_{o1} and its image is formed at the image distance s_{i1} both to L_1 normal plane. This image forms an object for L_2 with s_{o2} the object distance and s_{i2} the distance separating the normal plane of L_2 with the sample. $ØS$ is the spot size. The distances measured from the focal points with the object and image distance are defined as x_o and x_i for the object and image respectively.

Snell's law, θ_{max} can be calculated for optical fibers as,

$$\sin(\theta_{max}) = \frac{1}{n_i} NA \tag{5}$$

with n_i the refractive index of the incident medium index. In most cases, it is simply air and $n_i = n_{air} = 1.00028 \approx 1$. Similar to NA, f/# is given by the supplier and depends on lens focal length f and diameter D,

$$f/\# = \frac{f}{D} \approx \frac{1}{2(NA)} \tag{6}$$

Making use of trigonometry relations, the equation (6) can be rearranged with θ_{max} to the following expression.

$$\tan(\theta_{max}) = \frac{1}{2 n_i f/\#} \tag{7}$$

The geometrical parameters for optical fibers and lenses are represented Fig. 3.

By definition, θ_{max} is related to the divergence cone of the optical component. To calculate G, θ_{max} is converted into a solid angle Ω as a spherical cap.

$$\Omega = 2\pi(1 - \cos(\theta_{max})) \tag{8}$$

Finally, the throughput G is the product of the solid angle Ω of the optical component by its diameter D as follows.

$$G = \pi\Omega\left(\frac{D}{2}\right)^2 \tag{9}$$

Hence, G can be illustrated (Fig. 4) as multiple spherical caps distributed over the area of lenses aperture and optical fibers entrance/exit and delineated by the divergence cones defined by θ_{max}.

2.4. Signal-to-noise ratio

The last key point to achieve space- and time-resolved (STR) UV–vis DRS is to have high S/N of the collected light with a proper choice of light source and intrinsic spectrometer parameters such as integration time and spectral time-based averaging.

The integration time is the length of time during which the CCD is exposed to photons. Increasing this time led to an increase in the accumulation of the charges on the pixels due to an increase in photons exposure. However, if the number of charges exceeds the CCD saturation limit called as pixel well depth, spectrum will present characteristic features of the light source which take over the features of the sample on its spectrum. Time-based averaging calculates an average of each pixel information over the number of spectral acquisitions (i.e., spectral scans). On the one hand, by increasing the integration time without exceeding the saturation limit, the photon count of the signal from the sample raises and the other hand, by increasing the time-based averaging, the oscillation of the signal from the multiple sources of noise (i.e., photon noise, dark noise, electronic noise, etc.) is reduced. Therefore, S/N can be enhanced by increasing both integration time and time-based averaging.

In addition, the choice of the light source has strong effects on the quality of the S/N regarding first, its intensity which determines the intensity of the diffuse reflected light and second, its discrete or continuous emission spectrum which leads to a tendency for the CCD to saturate in the intense light regions. Herein, deuterium-halogen lamp (AVALIGHT-D-B-DUV and AVALIGHT-DH-B, Avantes) and high-pressure mercury lamp (SwiftCure PLU10 – UV Consulting Peschl) were tested as light sources, and their performances were compared (Fig. 5). Deuterium-halogen lamp has a smooth emission spectrum (apart from the deuterium characteristic Balmer lines D_β at 486 nm and D_α at 656 nm) in the range of 200–2500 nm favorable for UV–vis broadband spectroscopy, but its intensity is relatively weak making its use for diffuse reflectance methodologies challenging. Unlike deuterium-halogen lamp, high-pressure mercury lamp has a higher UV–vis intensity and is therefore often used for photocatalysis. However, its discrete emission spectrum leads to the saturation of the detector at the characteristic mercury emission lines.

Emission spectra of both lamps are compared in Fig. 5 based on the integration time value which leads to the start of CCD saturation. This information helps to evaluate the quality of S/N for time-resolved studies. For instance, high time-resolution can be achieved by setting small integration time. High-pressure mercury lamp enables to attain a good signal with a small integration time of 20 ms due to its great intensity whereas deuterium-halogen lamp requires a minimum of 260 ms integration time. Therefore, the high-pressure mercury lamp can be interesting to study fast catalytic processes that require short time resolution; however, this choice compromises spectral quality due to unavoidable effects of the CCD saturation. The deuterium-halogen lamp is more suitable for high spectral quality applications thanks to its continuous emission spectrum but compromises for lower time-resolution.

2.5. STR UV–vis DRS setup

A schematic drawing of the complete setup is shown in Fig. 6. As explained earlier, deuterium-halogen lamp and high-pressure mercury lamp were used as light sources. The light source is then coupled to a multi-mode optical fiber (FC-UV1000–1-BX-SR, Avantes, 0.22 NA, <100 °C, step-index fiber) with 600 μm diameter leading to a throughput value of 0.174 mm^2.sr. A collimating lens (FOA-COL-SMA, Lewvak, fused silica) fixed at the probe exit avoids the divergence of the incident light and therefore ensures a homogeneous irradiation onto the catalyst bed and prevents great losses of incident light. Its focal length is

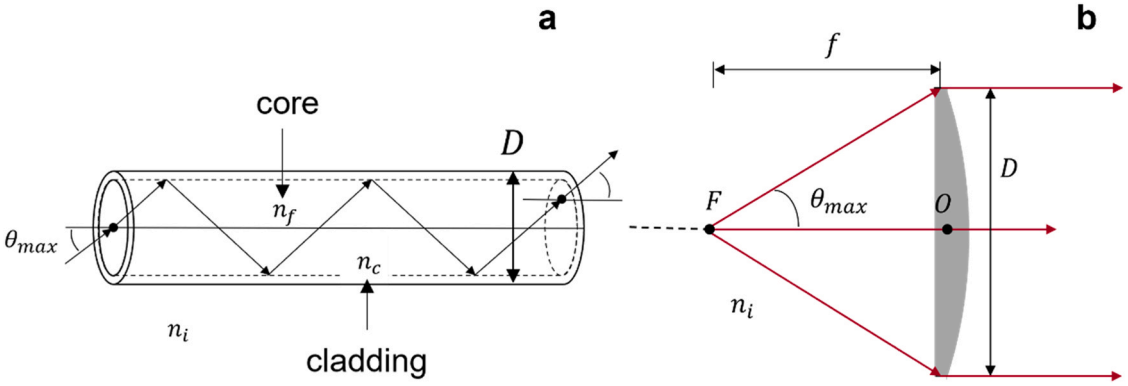

Fig. 3. (a) Rays entering with θ_{max} and undergoing total reflection in a clad optical fiber. (b) Rays entering with θ_{max} and undergoing refraction in a plano-convex lens.

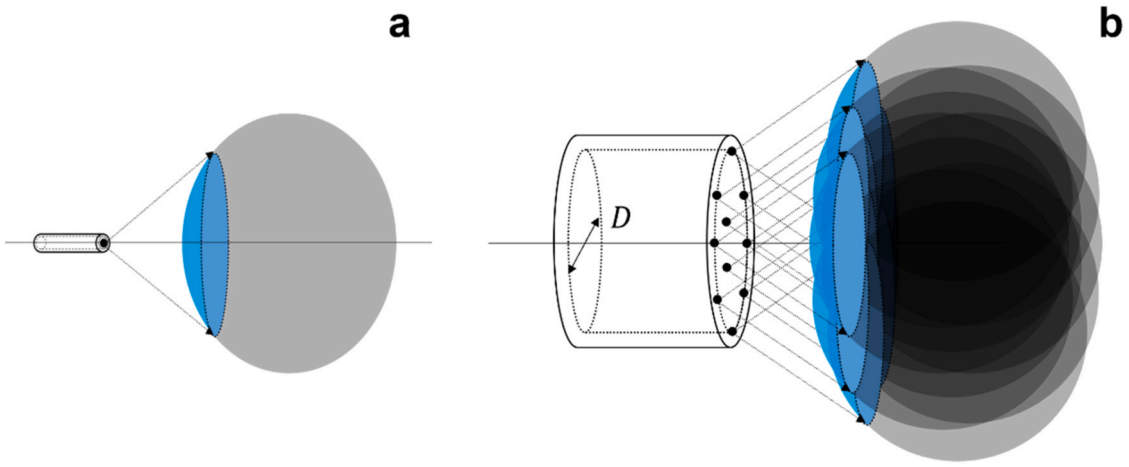

Fig. 4. Illustrations of the throughput (blue hemisphere), (a) for a thin optical fiber, (b) for a large optical fiber.

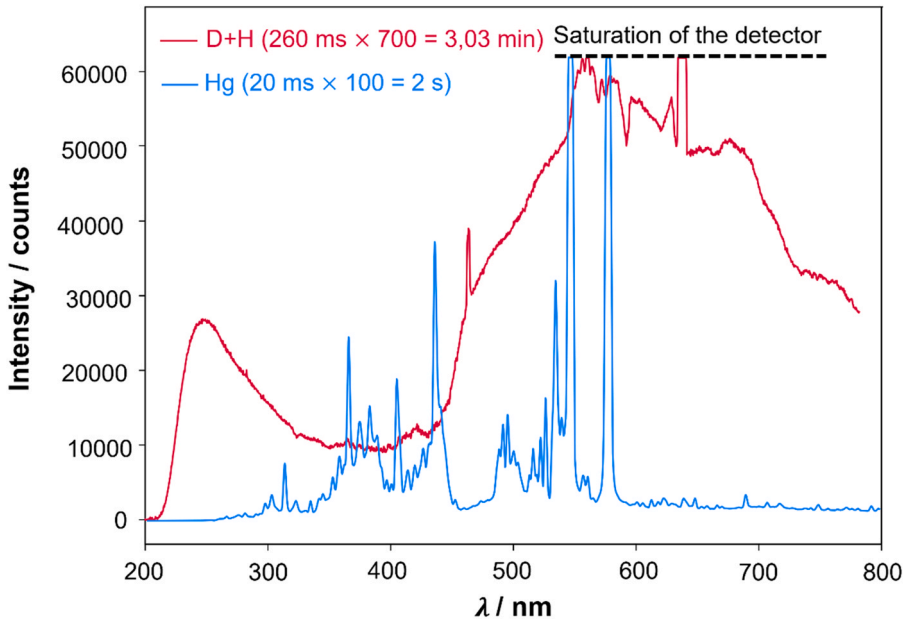

Fig. 5. Emission spectra of deuterium halogen (D+H) lamp collected with an integration time of 260 ms and averaged 700, i.e., 3 min time resolution, versus high-pressure mercury (Hg) lamp collected with an integration of 20 ms and averaged 100, i.e., 2 s time resolution.

11.99 mm, and its diameter is 4.06 mm, leading to a G value of 4.74 mm^2.sr. The probe and collimating lens gathering the incident light are placed at the angle of incidence α for the reasons described in Section 2.1.

Then, the diffuse reflected light is collected perpendicularly to the catalyst bed thanks to the combination of a collimating lens (L_1) (COL-UVVIS-25, Avantes, fused silica) with a plano-convex lens (L_2) (G063339000, Qioptic, fused silica). Alternatively, the setup could be mounted such that the combination of lenses is placed at the angle α while the incident light system is fixed perpendicular to the catalyst bed. However, the tubular interface of the reactor does not allow achieving a small and accurate spot size with the combination of lenses placed at α due to geometrical principles. Therefore, this reversed setup was not chosen for further development. Afterwards, L_1 was chosen for its variable focal length from 54 mm to 71 mm offering flexibility in the optimization of M_T (Eq. (2)). Similarly, L_2 was chosen for its focal length that enables to fix the lenses combination far enough from the reactor to avoid the heating of the optical components while the reactor is being heated. The focal length is refractive index-wavelength dependent, hence f_2 is in the range from 49.42 mm to 55.85 mm belonging to the wavelength range from 193 nm to 1064 nm. L_1 and L_2 have a throughput of 0.6380 mm^2.sr and 52.24 mm^2.sr, respectively. At the output of L_1, the light is gathered by the collection optical fiber (FC-UV1000–1-BX-SR, Avantes, 0.22 NA, $<$ 100 °C, step-index fiber) with 600 μm diameter leading to a G value of 0.174 mm^2.sr.

In this described OS, the throughput values of all the optical components were gathered and compared and the optical fibers present the smallest G value. Therefore, they limit the OS in terms of luminosity and this limit can only be enhanced by increasing their diameter ($ØD$) (Eq. (9)). However, increasing their diameter led to the increase of the spot size (Eq. (3)) hence, for our applications, the optimum was found for optical fibers of 600 μm $ØD$. In that way, a spot size of 1 mm could be measured within the wavelength range of visible light by adjusting L_1 focal length to form an optic 1:1, i.e., the focal lengths are equals thus there is no magnification of the collection fiber exit $ØD$.

Finally, the collection fiber is connected to the spectrometer (AvaSpec-3648-USB2, Avantes) with CCD linear array (TOSHIBA 3648), at a resolution of 5.2 s (260 ms × 20) with deuterium-halogen light source

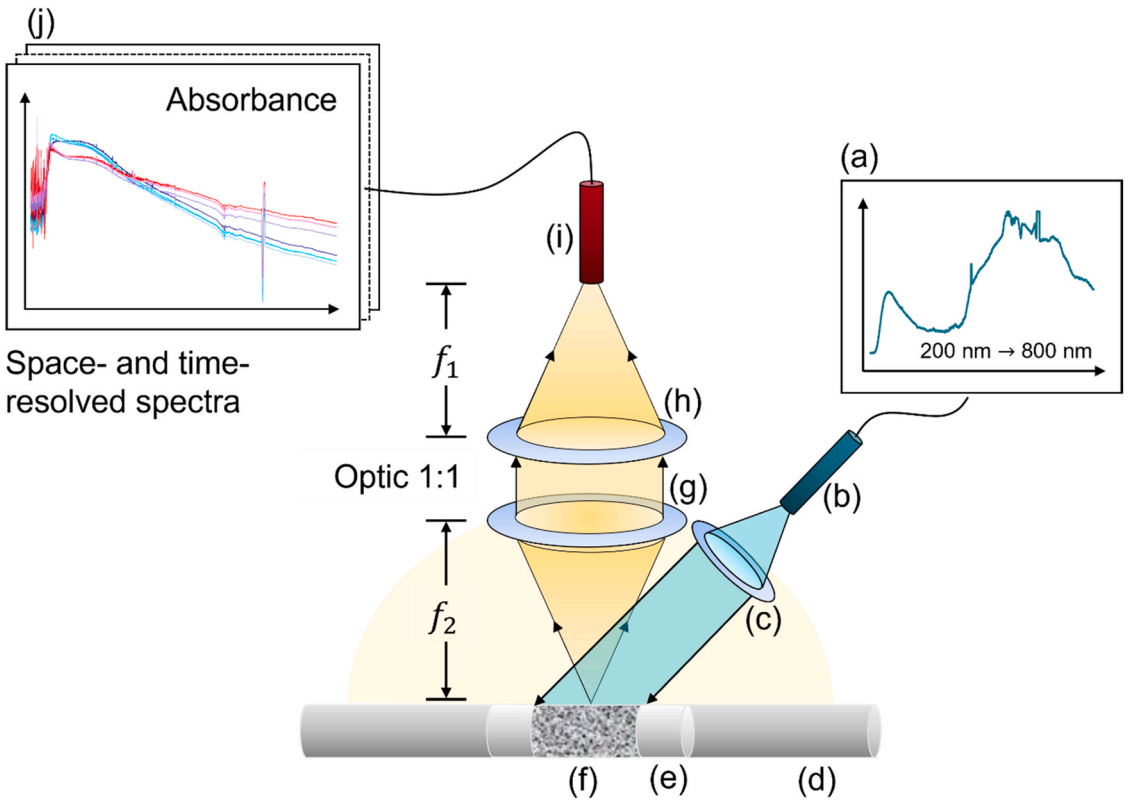

Fig. 6. Schematic drawing of the experimental setup within blue the incident light and in yellow the diffuse reflected light. (a) deuterium-halogen light source or high-pressure mercury lamp, (b) optical fiber of 600 μm diameter core, (c) incident collimating lens, (d) quartz reactor tube, (c) quart wool holding the catalytic bed in the tube, (f) catalyst materials, (g) plano-convex lens (L_2), (h), collection collimating lens (L_1), (i) collection fiber of 600 μm diameter core, (j) UV–vis spectrometer.

and 1.35 s (2.7 ms × 500) with high-pressure Mercury lamp to achieve high S/N.

2.6. Proof of principle: benchmark experiment for spatial resolution

In order to prove the UV–vis DRS setup capabilities for space-resolved experiments, the tubular quartz reactor was filled with a sequence of three colorful samples and was scanned along axial direction by the UV–vis spectrometer. At the interface region between two components, the expected UV–vis spectrum should present the contribution in absorption bands of both chemicals hence proving the spatial resolution of the instrument. Copper(II) chloride dihydrate (a), benzophenone-4.4′-dicarboxylic acid (b) and erioglaucine disodium salt (c) were selected for this study for their strong absorption bands in the UV–vis region that were clearly distinguishable from one to the other. For this study, high-pressure mercury lamp ensured the excitation of the chemicals while the location of the sample bed was changed along the axial direction by connecting the whole quartz reactor to a motorized motion system. A time resolution of 1.35 s could be achieved with a good S/N.

The UV–vis DR spectra from the region containing the pure chemical show the expected pure spectra with their characteristic absorption bands (Fig. 7a-c). On the other hand, the UV–vis DR spectra from the two interface regions at 5.2 mm and 10 mm clearly show a combination of spectral features from each chemical hence proving the spatial resolution of the setup.

3. CO oxidation over Pt/Al_2O_3: experimental methods

3.1. Catalyst synthesis

3 wt % Pt was supported on γ-Al_2O_3 (Thermo Fisher) by wet impregnation method using tetraammine platinum (II) nitrate (Sigma Aldrich, >99.995 %) as precursor. The resulting mixture was dried overnight at 80 °C and then calcined at 400 °C for 3 h.

3.2. CO oxidation: space-resolved gas sampling and temperature measurements

Catalytic tests were performed in a continuous flow fixed-bed reactor with 66 mg of the catalyst pellet with a sieved fraction of 100–300 μm. The catalyst was placed in a quartz reactor (I.D.: 4 mm, O.D.: 6 mm) and the bed length was 7 mm. The reaction was performed under steady state (2.5 % CO, 10 % O_2 in He, total flow: 100 mL/min) at temperatures of 150 and 200 °C, maintaining the reaction temperature within ± 2 °C using a heat gun in a housing to keep the reactor temperature homogenous from all directions. Prior to the experiments, the catalyst was pretreated with 5 % H_2/Ar at 300 °C for 1 h. Catalytic tests were also performed under unsteady state conditions, consisting of reduction phase (2.5 % CO in He, total flow: 100 mL/min, 150 s) and oxidation phase (10 % O_2 in He, total flow: 100 mL/min, 150 s) at 200 °C. Switching between the two phases was enabled by a 4-way value controlled by LabVIEW. To avoid the pressure fluctuation due to valve switching, the pressure of the exhaust stream at the 4-way valve was kept same as that of the reactor outlet by equalizing the pressure drops using a metering valve. The outlet gas composition was measured by transmission Fourier transform infrared spectroscopy (FT-IR, ALPHA, Bruker).

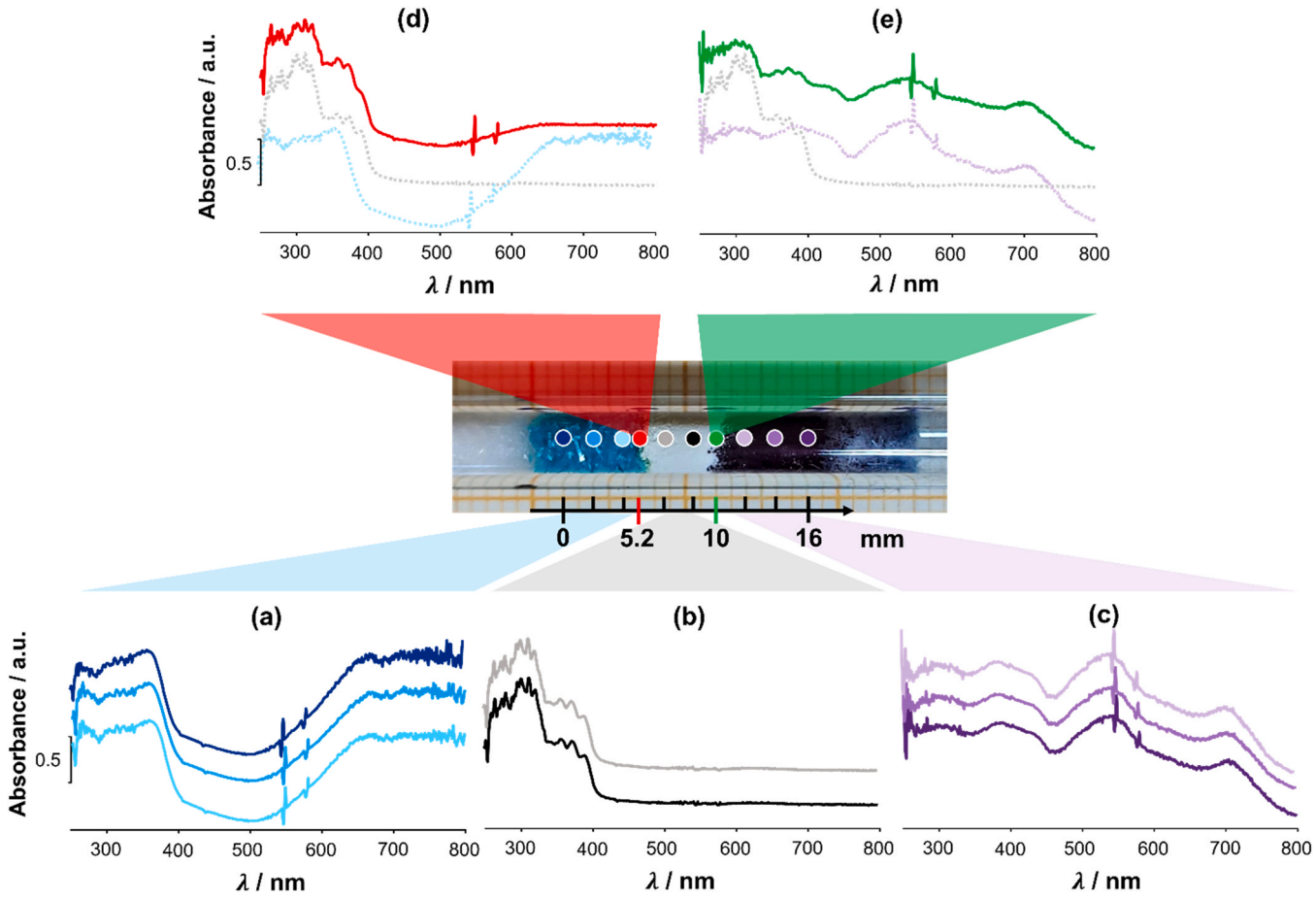

Fig. 7. Space-resolved UV–vis spectra demonstrating the sufficient resolution to study materials in the catalytic reactor. The spectra were measured on the spots represented on the quartz tube with their corresponding colors. Barium sulfate was used as the reference. The pure spectra in the single component region are showed in (a), Copper(II) chloride dihydrate, (b) benzophenone-4.4′-dicarboxylic acid, and (c), erioglaucine disodium salt. The spectra measured at the interface region are showed in (d) and (e) where the doted lines present the spectra from the spots next to the interface.

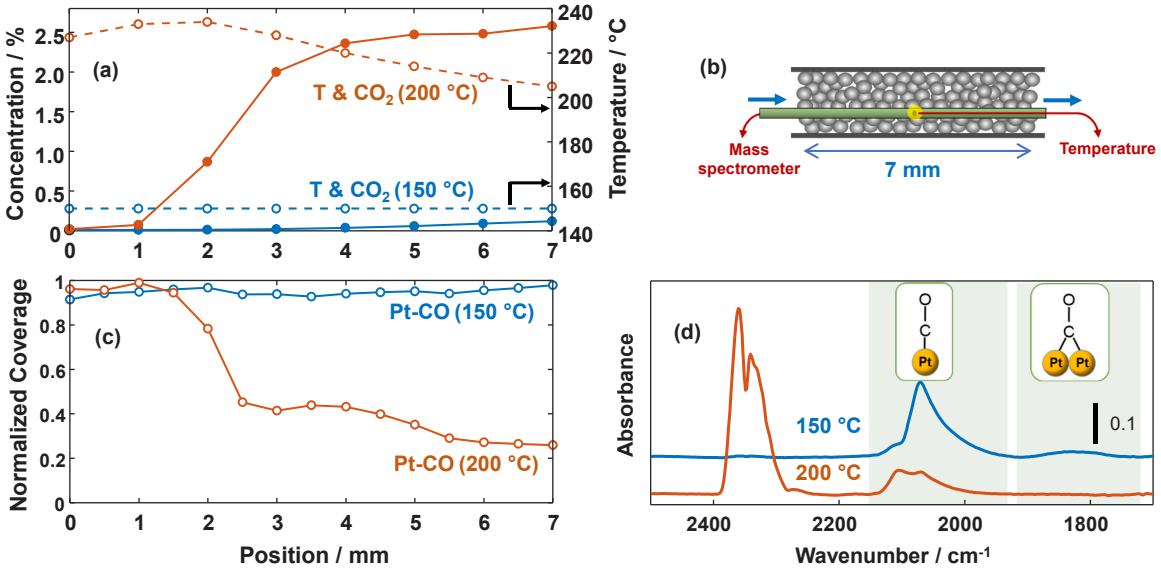

Fig. 8. (a) Spatial concentration (solid) and temperature (dotted) profiles at 150 (blue) and 200 °C (orange), (b) Schematic showing gas sampling set up, (c) Normalized coverage of adsorbed CO at 150 (blue) an 200 °C (orange), (d) DRIFT spectra recorded over Pt/Al_2O_3 at 150 and 200 °C. Conditions: 2.5 % CO, 10 % O_2 in He, total flow: 100 mL/min, 66 mg Pt/Al_2O_3.

Spatially resolved gas and temperature sampling, shown by the experimental setup schematic in Fig. 8b, was obtained by inserting a stainless steel capillary (I.D.: 500 μm, O.D.: 700 μm, REACNOSTICS GmbH), with four diagonal sampling holes (50 μm) and a K-type thermocouple inside the capillary aligned with the holes, through the center of the catalyst bed. The capillary was controlled bi-directionally using movable stages equipped with actuators of < 1 μm accuracy. A mass spectrometer (Omnistar Pfeiffer Vacuum) was connected to the outlet of the capillary to measure the gas composition passing through the holes from the catalyst bed at intervals of 1 mm.

3.3. Operando DRIFTS

Space-resolved steady-state spectra were acquired using a custom-made cell as previously reported [28,29]. The DRIFTS cell was placed inside a Harrick Praying Mantis optical accessory and the measurements were performed using Bruker INVENIO R FT-IR spectrometer, equipped with a LN-MCT detector, at a resolution of 4 cm^{-1}. Spectra recorded at steady state (under same operating conditions as catalytic studies) were an average of 800 scans at 40 kHz, taken at 0.5 mm intervals across the catalyst bed. Background reference spectra were collected after the reduction pretreatment (5 % H_2/Ar, 300 °C, 1 h) before starting DRIFTS measurements under CO adsorption (2.5 % CO, total flow: 100 mL/min) and reaction conditions (2.5 % CO, 10 % O_2 in He, total flow: 100 mL/min). The effluent gas mixture was analyzed by transmission FT-IR spectroscopy (ALPHA, Bruker).

3.4. Operando UV–vis DRS

Spatiotemporal UV–vis spectroscopy was performed using the configuration described above. A 600 μm fibre coupled with a collimating lens (Avantes, FOA-COL-SMA, Lewvak, fused silica) guided the incident light from the deuterium-halogen light source. Another 600 μm fibre coupled with an assembly of a collimating lens (COL-UVVIS-25, Avantes, fused silica) and a plano-convex lens (Avantes, G063339000, Qioptic) was used to guide the diffused reflected light to an Avantes UV–vis spectrometer (AvaSpec-3648–2USB2). A measurement time of 4.5 min was used for the steady-state measurements. For unsteady-state measurements, a time resolution of 5 s was used. The spectra plotted here were averaged over multiple cycles to attain high S/N. The operating conditions for steady- and unsteady-state were identical to the catalytic tests. The effluent gas mixture was analysed by transmission FT-IR spectroscopy (ALPHA, Bruker).

4. CO oxidation over Pt/Al_2O_3: results and discussion

4.1. Space-resolved operando methodologies applied for CO oxidation on Pt/Al_2O_3 under steady-state conditions

CO oxidation over Pt/Al_2O_3 is widely studied in the field of heterogenous catalysis due to its simplicity and practical significance [30,31]. In this work, we have selected it as the model reaction to illustrate the potential of *operando* UV–vis setup in extracting the information about Pt redox state. Pt serves as the active site for CO oxidation, while Al_2O_3 acts as an irreducible and inactive support facilitating the dispersion of Pt particles [32]. In the synthesized sample, the dispersion of Pt was found to be 26 % from CO pulsed chemisorption measurements (details in Supplementary Material).

Conventionally, insights into the reaction mechanisms and pathways are offered by the analysis of effluent gas composition. However, such analyses solely based on the outlet concentration can be misleading due to the existence of potential concentration (gas and surface species) and temperature variations in the reactor, which can have significant impact on the reaction mechanism, as indicated in previous studies [33]. Therefore, in this work, space-resolved techniques for gas sampling, temperature measurement and DRIFTS were employed to study CO oxidation over Pt/Al_2O_3 and identify the spatial variations gas and surface species and temperature, and their correlations. As the unique information of the developed UV–vis DRS, we complement the information by highlighting the dynamics and gradient of Pt redox state in the reactor.

The analysis of the outlet gas concentration revealed CO conversion of 4 % and 99 % at 150 and 200 °C, respectively. Fig. 8a shows the concentration profile of CO_2 formed at different axial position across the catalyst bed at 150 (blue) and 200 °C (orange) and the schematic of the setup is shown in Fig. 8b. The spatial concentration and temperature profiles (Fig. 8a) show no significant formation of CO_2 at 150 °C, and consequently, no detectable temperature rise was observed due to the minor exothermicity. In contrast, at 200 °C prominent CO_2 formation was observed between 1 and 4 mm of the catalyst bed. This CO_2 concentration increase was accompanied by a temperature rise due to the exothermicity of the reaction. Fig. S1 clearly depicts that the highest CO_2 formation occurred between 1 and 3 mm with a maximum temperature rise of 34 °C at 2 mm. Nearly 99 % CO conversion was observed at 4 mm which defines the CO oxidation activity over Pt/Al_2O_3 at 200 °C before this position of the catalyst bed.

To understand the gradient in the coverage of CO on Pt across the catalyst bed, space-resolved DRIFTS measurements were performed over Pt/Al_2O_3 at 150 and 200 °C. DRIFT spectra recorded under reaction conditions (one example at 150 °C, Fig. 8d) show a sharp band at 2069 cm^{-1} and a weaker band at 2106 cm^{-1} associated to CO linearly adsorbed to defect Pt (step, edge) and terrace Pt, respectively [34]. A broader band at 1825 cm^{-1} was assigned to bridged Pt-CO species [34]. Fig. 8c shows the spatial variation of normalized coverage of combined Pt-CO (atop and bridged) species assuming that the absorption cross sections of CO stretching vibrations of all differently adsorbed CO species on Pt are identical. The method of calculating normalized coverage is crucial to compare the signals from the different axial positions and it is detailed in the supplementary information (Fig. S2). It is clear from Fig. 8c that the normalized coverage of CO on Pt was ca. 1 at 150 °C at all positions, indicating that the Pt surface was effectively covered by CO and that the surface was largely poisoned and inaccessible for O_2 dissociative adsorption. This explains the negligible CO_2 formation (Fig. 8a). At 200 °C, the normalized CO coverage was ca. 1 between 0 and 1 mm and decreased along the axial direction of the catalyst bed correlating with the increase in CO_2(g) formation and rise in temperature (Fig. 8a). As CO approached full conversion at > 4 mm, the 2106 cm^{-1} terrace Pt-CO band became more dominant adsorbed species, with defect and bridge species largely depleted (Fig. 8d). The presence of Pt-CO species indirectly informs about the redox state of Pt, as CO is expected to adsorb to metallic Pt while it is immediately oxidized when Pt is oxidized, possibly with the presence of reactive PtO_x islands on Pt surface [35,36]. The depletion of CO adsorbed on defect sites and stability of CO adsorbed on terrace sites suggest an increased oxidation of Pt at step-edges and preferential retention of metallic Pt on the terraces.

The space-resolved study of CO oxidation over Pt/Al_2O_3 by DRIFTS, gas sampling and temperature profiling suggest that the nature of active sites can vary and alter in space, depending on the reaction temperature. Specifically, it was indicated that Pt is reduced throughout the catalyst bed by dominant CO coverage at 150 °C, whereas the Pt, initially reduced at the front position, gets oxidized in the highly reactive zone of the catalyst bed. This information can only be studied by *operando* methodologies because the state of the catalyst is unique; hence the common analytical techniques to study the redox state of chemical elements and metals such as X-ray photoemission spectroscopy cannot be used. Hard X-ray absorption spectroscopy is the method of choice. However, this requires commonly a synchrotron X-ray source. It is not convenient or not possible to perform such measurements under the identical conditions due to limited accessibility and optical constraints. To gain insights into the redox state of Pt, we employed the space-resolved UV–vis DRS developed in this work under *operando*

conditions. Importantly, the reactor and experimental conditions are identical to those used for gas sampling and temperature measurements, enabling simultaneous measurements and facilitating a multimodal mode of *operando* study.

Fig. 9 summarizes the results obtained by space-resolved UV–vis DRS during CO oxidation at 150 and 200 °C. Due to the rather small spectral changes, the UV–vis DR spectra are presented as difference spectra with reference to the reduced state of Pt/Al_2O_3. In other words, if the spectral feature is none (i.e., straight line around zero intensity), this implies that Pt is in the reduced metallic state. First, to evaluate if UV–vis DRS is able to differentiate the redox states of Pt, we oxidized Pt/Al_2O_3 by passing 10 % O_2 at 150 and 200 °C. The black lines in Fig. 9 show the spectra recorded under the oxygen atmosphere, clearly demonstrating the increased absorbance below ca. 250 and above 350 nm, whereas the absorbance decreases between 250 and 350 nm with respect to the reduced state of Pt. The spectral features of the catalyst under the oxidizing condition are consistent at all positions and at the two temperatures. A more careful look shows that the spectral changes at 200 °C is more prominent than those at 150 °C with even more negative absorption at 260–270 nm. This is indicative of higher degree of Pt oxidation or more bulk oxidation. This degree of Pt oxidation or the state of Pt oxide is one of the most critical aspects to understand the active sites for CO oxidation, but this elucidation is out of the scope of this work and for future studies. Here, we interpret the oxidized state of Pt qualitatively.

Under CO oxidation (Fig. 9), the difference spectra underwent changes as expected. The spectra obtained at 150 °C (indicated by the blue line) exhibit nearly straight-line profiles. As noted above, this indicates that Pt in the catalyst is in its reduced state during the CO oxidation at 150 °C throughout the catalyst bed, in accordance with the space-resolved DRIFTS results (Fig. 8c). On the other hand, at 200 °C (indicated by the red line) the redox state of Pt is close to the reduced state near the front position (0.5 mm), whereas the redox state changed to the oxidized state to the maximum extent defined by the oxygen concentration and temperature. The results are in perfect accordance with the space-resolved results presented in Fig. 8 and confirm that the normalized CO coverage is a good indicator of Pt redox state. The redox state of Pt changes in the reactor at 200 °C in the region where the CO_2 is most produced. The results imply also the change in nature of active sites within the reactor at 200 °C and consequently changes from Langmuir-Hinshelwood mechanism (reaction between adsorbed CO and dissociated oxygen on Pt) to Eley-Rideal or Mars-Van Krevelen mechanism where CO reacts readily with the reactive surface oxygen of oxidized Pt or with such oxygen species combined from the gas phase. Further studies are necessary to clarify the mechanisms, but the results show that it is important and necessary to take into account the exothermicity, inhomogeneous concentration gradients and active site variations to understand reactivity and that we need to be careful about these factors for kinetic studies where commonly homogenous active sites and reaction mechanisms are assumed.

4.2. *Space- and time-resolved operando UV–vis DRS applied for CO oxidation on Pt/Al_2O_3 under unsteady-state condition*

The above study demonstrates the capability of the developed setup to perform space-resolved UV–vis DRS. Therein, the Pt redox state information and its spatial variations were elucidated. Using the new tool developed, it is important to stress that the UV–vis spectra can be recorded in a highly time-resolved manner. When it is combined the space-resolved study, i.e. by translational movement of the probe or the reactor along the axial direction, we enable spatiotemporal *operando* UV–vis DRS study. The effective temporal resolution is typically limited not by the instrumental restrictions but rather by the S/N defined by the light source and light absorption by a sample. In this section, we describe

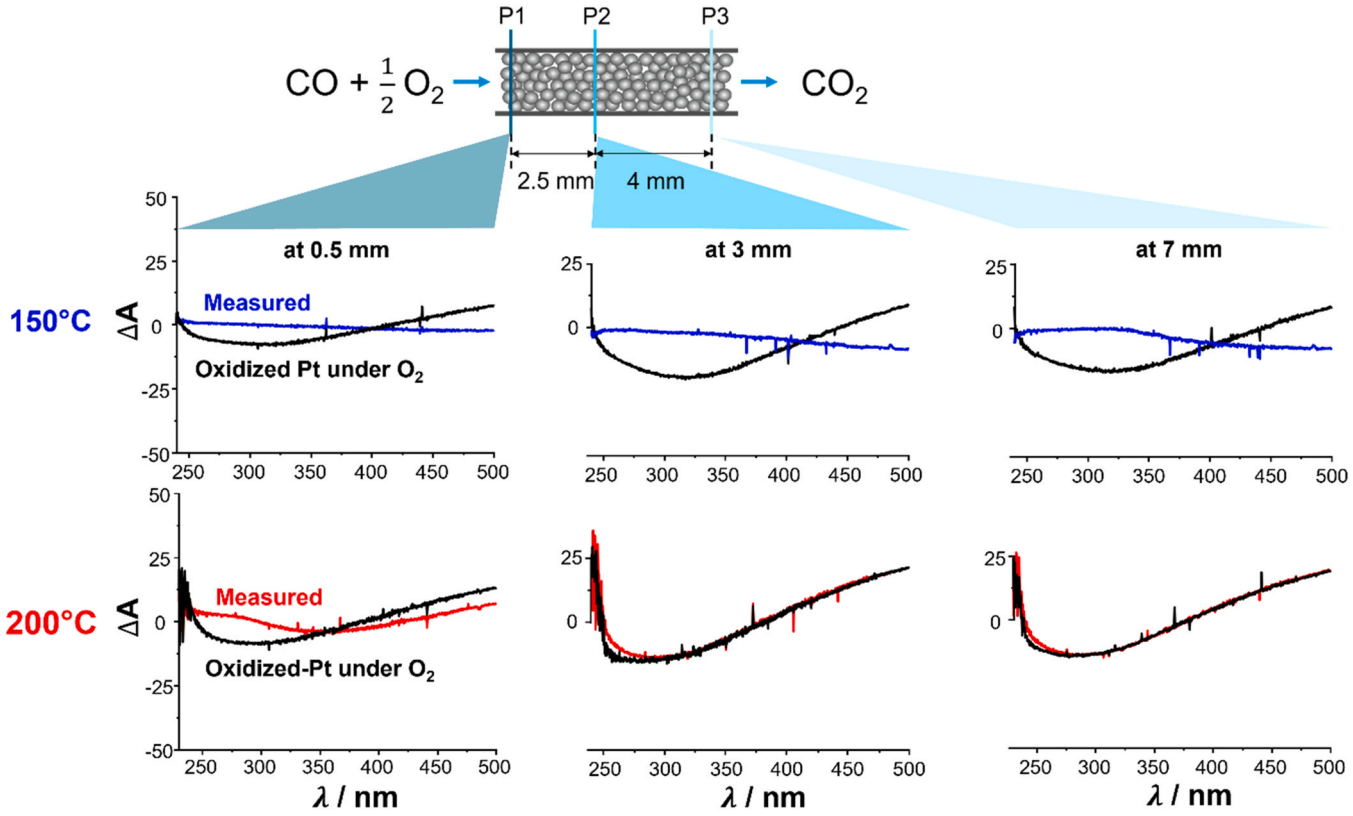

Fig. 9. Space-resolved UV–vis DR difference spectra during steady-state CO oxidation at 150 and 200 °C at three positions of the catalyst bed as indicated in the figure. The reference state is Pt/Al_2O_3 catalyst reduced by H_2 at 300 °C and recorded at the reaction temperature at respective positions. Conditions: 2.5 % CO, 10 % O_2 in He, total flow: 100 mL/min, 66 mg Pt/Al_2O_3, UV–vis Spectroscopy: time resolution 4.5 min, positions: 0.5 mm (P1), 3.0 mm (P2) and 7.0 mm (P3).

the use of the developed setup to perform spatiotemporal *operando* UV–vis DRS to elucidate the redox state of Pt under unsteady-state CO oxidation over Pt/Al_2O_3 at 200 °C by alternately passing 2.5 % CO and 10 % O_2 diluted in He to induce CO oxidation by adsorbed CO and surface atomic oxygen species. The time resolution of the spectra was 5 s, but the spectral quality was improved by averaging several CO vs. O_2 cycles after reaching the quasi-steady-state.

Fig. 10 presents the temporal evolution of the difference UV–vis DR spectra at 325 nm at three positions (P1-P3) along the catalyst bed. The wavelength was chosen because this region is sensitive to the redox state of Pt (Fig. 9). Apparently, the spectral response goes positive to negative upon switching the atmosphere from CO to O_2. This indicates that an oxidized state of Pt is formed by switching from CO to O_2 and this state is reversibly changed back to the metallic state upon switching back to CO. The results clearly show the capability of the developed setup for time-resolved studies. Furthermore, the spectral response at the three locations evidences that the spectral changes occurs sequentially from the more front position (P1) towards the back position (P3), as expected. This change of redox state from P1 to P3 takes about 10–20 s with slightly slower changes when switching from O_2 to CO compared to switching from CO to O_2. This implies that reduction of oxidized Pt takes more time at this temperature than oxidation of Pt. This study firmly demonstrates that the setup can be indeed used to study the variation of metal redox states in the catalytic reactor with time-resolution, offering great opportunities to investigate numerous systems in heterogenous catalysis, in combination with transient studies.

5. Conclusions

An optical fiber-based UV–vis DRS setup was designed to study the state of catalyst in a fixed-bed reactor with spatial resolution on the reactor scale. By collecting diffuse reflected light from a localized spot and enabling translational movement along the axial direction of the reactor, space-resolved studies became possible. When a bright light source is used, high time-resolution can be also achieved, allowing for spatiotemporal *operando* studies. The design of the setup is practical, as it was specifically tailored to study a tubular fixed-bed catalytic reactor. Thus, the catalytic performance and reaction conditions are not compromised during *operando* studies using this setup.

CO oxidation to CO_2 over Pt/Al_2O_3, operated under steady-state ($CO+O_2$ feed) and unsteady-state (periodic CO vs. O_2 feed), was chosen as the model reaction to validate the capabilities of the UV–vis DRS setup for heterogenous catalysis research. The information gained by space-resolved DRIFTS, gas sampling and temperature profiling were combined with the data obtained by UV–vis DRS. The results clearly show that Pt is reduced and fully covered by CO at 150 °C, hindering the adsorption, dissociation and thus activation of O_2 for CO oxidation and resulting in low CO conversion. In contrast, the oxidation state of Pt transitions from the metallic state to a more oxidized state, as observed through the coverage of CO in DRIFTS and directly confirmed by UV–vis DRS. Through space-resolved gas sampling and temperature profiling, the locations where the reaction takes place and exothermicity arises are elucidated. Furthermore, dynamic temporal changes in the Pt redox state were clearly observed by UV–vis DRS during CO oxidation under unsteady-state operation. By examining different locations within the catalyst bed, the movement of the Pt redox front and its timing within the catalyst bed were elucidated. The developed UV–vis DRS setup provides new opportunities for multimodal *operando* studies, offering both space- and time-resolution.

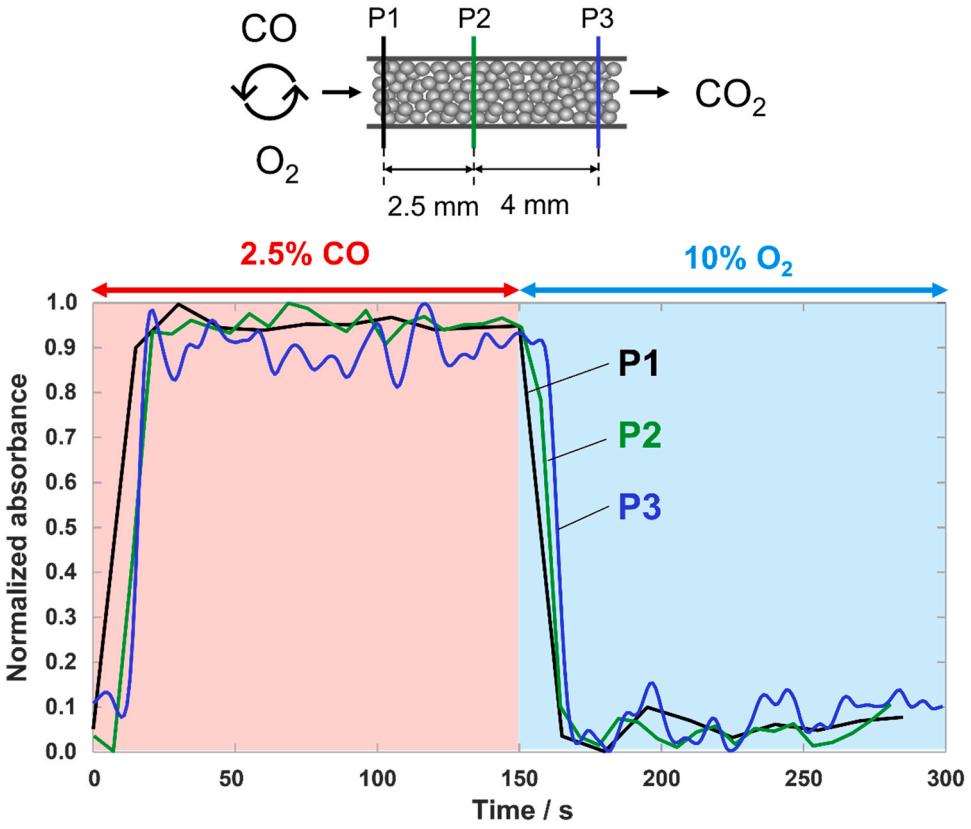

Fig. 10. Temporal evolution of normalized absorbance at 325 nm of UV–vis DR difference spectra referenced to the reduced state of Pt/Al_2O_3 measured at three positions of the catalyst bed as indicated in the figure during unsteady-state CO oxidation by alternately passing CO and O_2 over Pt/Al_2O_3. Conditions: 2.5 % CO in He vs. 10 % O_2 in He, total flow: 100 mL/min, 66 mg Pt/Al_2O_3. UV-vis spectroscopy: time resolution 5 s, positions: 0.5 mm (P1), 3.0 mm (P2) and 7.0 mm (P3).

Declaration of Competing Interest

The authors declare that they have no known competing financial interests or personal relationships that could have appeared to influence the work reported in this paper.

Data Availability

Data will be made available on request.

Appendix A. Supporting information

Supplementary data associated with this article can be found in the online version at doi:10.1016/j.cattod.2023.114466.

References

[1] B.M. Weckhuysen, Determining the active site in a catalytic process: operando spectroscopy is more than a buzzword, J. Phys. Chem. Chem. Phys. 5 (2003) 4351–4360.
[2] M.A. Bañares, Operando methodology: combination of in situ spectroscopy and simultaneous activity measurements under catalytic reaction conditions, Catal. Today 100 (2005) 71–77.
[3] A. Urakawa, A. Baiker, Space-resolved profiling relevant in heterogeneous catalysis, Top. Catal. 52 (2009) 1312–1322.
[4] A. Urakawa, Trends and advances in operando methodology, Curr. Opin. Chem. Eng. 12 (2016) 31–36.
[5] A. Vamvakeros, D. Matras, S.D.M. Jacques, M. di Michiel, S.W.T. Price, P. Senecal, M.A. Aran, V. Middelkoop, G.B.G. Stenning, J.F.W. Mosselmans, I.Z. Ismagilov, A. M. Beale, Real-time multi-length scale chemical tomography of fixed bed reactors during the oxidative coupling of methane reaction, J. Catal. 386 (2020) 39–52.
[6] M.A. Bañares, M. Daturi, Understanding catalysts by time-/space-resolved operando methodologies, Catal. Today 423 (2023), 114255.
[7] A.N. Pestryakov, N. Bogdanchikova, A. Simakov, I. Tuzovskaya, F. Jentoft, M. Farias, A. Díaz, Catalytically active gold clusters and nanoparticles for CO oxidation, Surf. Sci. 601 (2007) 3792–3795.
[8] E. Kolobova, A. Pestryakov, G. Mamontov, Y. Kotolevich, N. Bogdanchikova, M. Farias, A. Vosmerikov, L. Vosmerikova, V. Cortes, Corberan, Low-temperature CO oxidation on Ag/ZSM-5 catalysts: Influence of Si/Al ratio and redox pretreatments on formation of silver active sites, Fuel 188 (2017) 121–131.
[9] J. Goetze, F. Meirer, I. Yarulina, J. Gascon, F. Kapteijn, J. Ruiz-Martínez, B. M. Weckhuysen, Insights into the activity and deactivation of the methanol-to-olefins process over different small-pore zeolites as studied with operando UV–vis spectroscopy, ACS Catal. 7 (2017) 4033–4046.
[10] X. Gao, M.A. Banares, I.E. Wachs, Ethane and n-butane oxidation over supported vanadium oxide catalysts: an in situ UV–visible diffuse reflectance spectroscopic investigation, J. Catal. 188 (1999) 325–331.
[11] P. Rybarczyk, H. Berndt, J. Radnik, M.-M. Pohl, O. Buyevskaya, M. Baerns, A. Brückner, The structure of active sites in Me–V–O catalysts (Me= Mg, Zn, Pb) and its influence on the catalytic performance in the oxidative dehydrogenation (ODH) of propane, J. Catal. 202 (2001) 45–58.
[12] B.M. Weckhuysen, A.A. Verberckmoes, J. Debaere, K. Ooms, I. Langhans, R. A. Schoonheydt, In situ UV–Vis diffuse reflectance spectroscopy—on line activity measurements of supported chromium oxide catalysts: relating isobutane dehydrogenation activity with Cr-speciation via experimental design, J. Mol. Catal. A: Chem. 151 (2000) 115–131.
[13] X. Gao, J.-M. Jehng, I.E. Wachs, In situ UV–vis–NIR diffuse reflectance and Raman spectroscopic studies of propane oxidation over ZrO_2-supported vanadium oxide catalysts, J. Catal. 209 (2002) 43–50.
[14] A. Bensalem, B.M. Weckhuysen, R.A. Schoonheydt, In situ diffuse reflectance spectroscopy of supported chromium oxide catalysts: kinetics of the reduction process with carbon monoxide, J. Phys. Chem. B 101 (1997) 2824–2829.
[15] J. Melsheimer, M. Thiede, R. Ahmad, G. Tzolova-Müller, F.C. Jentoft, Improved experimental setup for in situ UV–vis–NIR spectroscopy under catalytic conditions, J. Phys. Chem. Chem. Phys. 5 (2003) 4366–4370.
[16] A. Brückner, Simultaneous combination of in situ-EPR/UV–VIS/on line GC: a novel setup for investigating transition metal oxide catalysts under working conditions, Chem. Commun. (2001) 2122–2123.
[17] R. Philipps, S. Walter, M. Liauw, Selective oxidation of isoprene to citraconic anhydride, Chem. Eng. J. 90 (2002) 107–116.
[18] A.M. Beale, A.M.J. van der Eerden, K. Kervinen, M.A. Newton, B.M. Weckhuysen, Adding a third dimension to operando spectroscopy: a combined UV-Vis, Raman and XAFS setup to study heterogeneous catalysts under working conditions, Chem. Commun. (2005) 3015–3017.
[19] C.T. Nottbohm, C. Hess, Investigation of ceria by combined Raman, UV–vis and X-ray photoelectron spectroscopy, Catal. Commun. 22 (2012) 39–42.
[20] T.A. Nijhuis, S.J. Tinnemans, T. Visser, B.M. Weckhuysen, Towards real-time spectroscopic process control for the dehydrogenation of propane over supported chromium oxide catalysts, Chem. Eng. Sci. 59 (2004) 5487–5492.
[21] J. Sattler, I. Gonzalez-Jimenez, A. Mens, M. Arias, T. Visser, B. Weckhuysen, Operando UV-Vis spectroscopy of a catalytic solid in a pilot-scale reactor: deactivation of a CrO_x/Al_2O_3 propane dehydrogenation catalyst, Chem. Commun. 49 (2013) 1518–1520.
[22] R.L. Puurunen, B.G. Beheydt, B.M. Weckhuysen, Monitoring chromia/alumina catalysts in situ during propane dehydrogenation by optical fiber UV–visible diffuse reflectance spectroscopy, J. Catal. 204 (2001) 253–257.
[23] E. Hecht, Geom. Opt., Opt. (2002) 149–242.
[24] H. Zhu, P. Blackborow, Etendue and optical throughput calculations, Energetiq Technologies Inc, Appl. Note Ref. (2011), 002-002.
[25] W. Hug, G. Hangartner, A novel high-throughput Raman spectrometer for polarization difference measurements, J. Raman Spectrosc. 30 (1999) 841–852.
[26] J.T. Meade, B.B. Behr, A.R. Hajian, A new high-resolution, high-throughput spectrometer: first experience as applied to Raman spectroscopy, Next-Generation Spectroscopic Technologies V. SPIE, 2012, pp. 242–249.
[27] C. Zhang, G. Li, T. Yan, X. Du, Y. Wang, The optical throughput of near-infrared static wind imaging interferometer, Opt. Commun. 498 (2021), 127227.
[28] A. Urakawa, N. Maeda, A. Baiker, Space- and time-resolved combined DRIFT and Raman Spectroscopy: monitoring dynamic surface and bulk processes during NOx storage reduction, Angew. Chem. Int. Ed. 47 (2008) 9256–9259.
[29] T. Hyakutake, W. van Beek, A. Urakawa, Unravelling the nature, evolution and spatial gradients of active species and active sites in the catalyst bed of unpromoted and K/Ba-promoted Cu/Al_2O_3 during CO_2 capture-reduction, J. Mater. Chem. A 4 (2016) 6878–6885.
[30] H.-J. Freund, G. Meijer, M. Scheffler, R. Schlögl, M. Wolf, CO oxidation as a prototypical reaction for heterogeneous processes, Angew. Chem. Int. Ed. 50 (2011) 10064–10094.
[31] A.D. Allian, K. Takanabe, K.L. Fujdala, X. Hao, T.J. Truex, J. Cai, C. Buda, M. Neurock, E. Iglesia, Chemisorption of CO and mechanism of CO oxidation on supported platinum nanoclusters, J. Am. Chem. Soc. 133 (2011) 4498–4517.
[32] H. Shinjoh, M. Hatanaka, Y. Nagai, T. Tanabe, N. Takahashi, T. Yoshida, Y. Miyake, Suppression of noble metal sintering based on the support anchoring effect and its application in automotive three-way catalysis, Top. Catal. 52 (2009) 1967–1971.
[33] A.M. Gänzler, M. Casapu, D.E. Doronkin, F. Maurer, P. Lott, P. Glatzel, M. Votsmeier, O. Deutschmann, J.-D. Grunwaldt, Unravelling the different reaction pathways for low temperature CO oxidation on Pt/CeO_2 and Pt/Al_2O_3 by spatially resolved structure–activity correlations, J. Phys. Chem. Lett. 10 (2019) 7698–7705.
[34] M.J. Kale, P. Christopher, Utilizing quantitative in situ FTIR spectroscopy to identify well-coordinated Pt atoms as the active site for CO oxidation on Al_2O_3-supported Pt catalysts, ACS Catal. 6 (2016) 5599–5609.
[35] B.L.M. Hendriksen, J.W.M. Frenken, CO oxidation on Pt(110): scanning tunneling microscopy inside a high-pressure flow reactor, Phys. Rev. Lett. 89 (2002), 046101.
[36] A. Urakawa, T. Bürgi, H.-P. Schläpfer, A. Baiker, Simultaneous in situ monitoring of surface and gas species and surface properties by modulation excitation polarization-modulation infrared reflection-absorption spectroscopy: CO oxidation over Pt film, J. Chem. Phys. (124) (2006).